Journal of Nuclear Materials 385 (2009) 424–430

Contents lists available at ScienceDirect

Journal of Nuclear Materials

journal homepage: www.elsevier.com/locate/jnucmat

Computed phase equilibria for burnable neutron absorbing materials for advanced pressurized heavy water reactors

E.C. Corcoran [a,*], B.J. Lewis [a], W.T. Thompson [a], J. Hood [b], F. Akbari [c], Z. He [c], P. Reid [b]

[a] Department of Chemistry and Chemical Engineering, Royal Military College of Canada, P.O. Box 17000, St. Forces, Kingston, Ont., Canada K7K 7B4
[b] Atomic Energy of Canada Ltd., Sheridan Park, 2251 Speakman Drive, Mississauga, Ont., Canada L5K 1B2
[c] Atomic Energy of Canada Ltd., Chalk River Laboratories, Chalk River, Ont., Canda K0J 1J0

A B S T R A C T

Burnable neutron absorbing materials are expected to be an integral part of the new fuel design for the Advanced CANDU®[CANDU is as a registered trademark of Atomic Energy of Canada Limited.] Reactor. The neutron absorbing material is composed of gadolinia and dysprosia dissolved in an inert cubic-fluorite yttria-stabilized zirconia matrix. A thermodynamic model based on Gibbs energy minimization has been created to provide estimated phase equilibria as a function of composition and temperature. This work includes some supporting experimental studies involving X-ray diffraction.

1. Introduction

Yttria-stabilized zirconia (YSZ) fuel materials have been studied extensively in Europe, Russia, Japan, and the United States as a means of decreasing stockpiles of plutonium and other actinide elements [1–5]. YSZ may also be studied as means of introducing neutron absorbing lanthanides for potential reactor control or an increase of safety margins. For these systems, fundamental thermodynamics can be applied to provide guidance of the most stable phases at specific conditions of composition and temperature [6,7]. This approach is especially useful at high temperature or high radiation fields where experimental work is difficult to conduct. Furthermore, it is applicable to multi-component systems such as the burnable neutron absorber (BNA) material proposed for the central element of the Advanced CANDU® Reactor (ACR) fuel bundle [8].

The BNA material for the ACR is proposed to be a mixture of gadolinia (Gd_2O_3 or $GdO_{1.5}$) and dysprosia (Dy_2O_3 or $DyO_{1.5}$), dissolved in an inert yttria (Y_2O_3 or $YO_{1.5}$) stabilized zirconia (ZrO_2) matrix. For simplicity, RE (for rare earth) will be used to represent Gd, Dy and Y. Although Y is not a true member of the rare earth series, it has a similar charge and ionic radius and therefore for the purpose of this paper will be grouped with chemically similar Gd and Dy.

As the BNA material does not have a broad experience base in pressurized heavy water reactors, a thermodynamic model is of use to facilitate composition selection, determine phase stability at reactor operation conditions, and predict aqueous solubility in the case of a sheathing breach. This paper highlights the methodology of Gibbs energy minimization, provides the thermodynamic data used to compute the phase model, and discusses X-ray diffraction experimentation to support phase stability computations at reactor operation conditions.

2. Modelling methodology

For this treatment, the binary systems, zirconia–gadolinia, zirconia–dysprosia, and zirconia–yttria were modelled from first principles to follow previously proposed diagrams found in the literature. A comparison between BNA binary subsets is presented and discussed. The binary systems were then incorporated into a cohesive quaternary model used to predict phase stability as a function of temperature and composition.

The binary ZrO_2–RE_2O_3 subsystems were modelled [9] as a preliminary construct to the quaternary system. To illustrate the thermodynamic fundamentals of Gibbs energy minimization [10], consider the ZrO_2–Gd_2O_3 binary system at 2773 K, where only cubic-fluorite and liquid phases may exist (Figs. 1 and 2). The phase(s) occurring at this temperature and composition must provide the largest reduction in Gibbs energy (ΔG) for the system, in relation to the Gibbs energy of a component mixture at the same temperature. For a binary system, the change in the Gibbs energy resultant from mixing and dissolution of the solid solution may be viewed as the summation of an ideal mixing term (ΔG_{ideal}) and an excess Gibbs energy term (G^E). The ideal mixing term assumes cations [Zr^{4+}, Gd^{3+}] in the binary system randomly interchange on similar lattice sites. For 1 mol of solution of ZrO_2–$GdO_{1.5}$ (where the Zr^{4+} and Gd^{3+} ions are in a 1:1 ratio), the ideal mixing may be represented by [6,10]:

$$\Delta G_{ideal} = x_{ZrO_2} RT \ln x_{ZrO_2} + x_{GdO_{1.5}} RT \ln x_{GdO_{1.5}}, \quad (1)$$

* Corresponding author. Tel.: +1 613 541 6000 3508; fax: +1 613 542 9489.
E-mail address: emily.corcoran@rmc.ca (E.C. Corcoran).

0022-3115/$ - see front matter Crown Copyright © 2008 Published by Elsevier B.V. All rights reserved.
doi:10.1016/j.jnucmat.2008.12.029

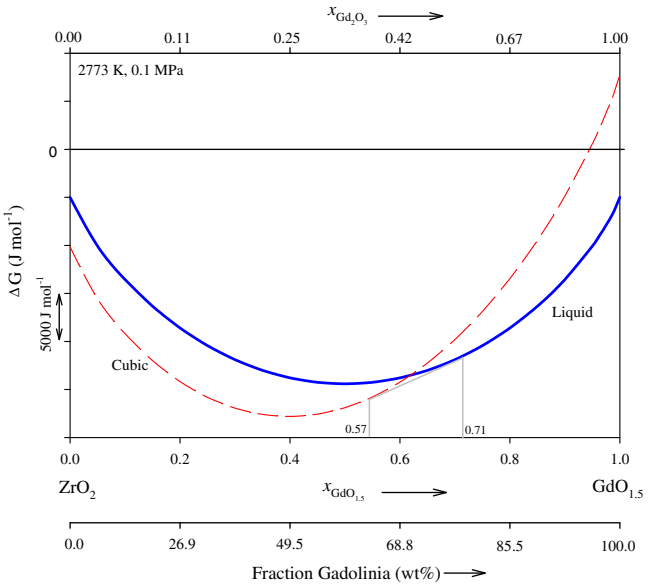

Fig. 1. Gibbs energy isothermals for cubic-fluorite and liquid phases at 2773 K and 0.1 MPa.

where x_{ZrO_2} and $x_{GdO_{1.5}}$ are the mol fractions of ZrO_2 and $GdO_{1.5}$, respectively, R is the ideal gas constant, and T is the absolute temperature (K). Equally, for a 1 mol solution of ZrO_2–Gd_2O_3, the ideal mixing term is

$$\Delta G_{ideal} = x_{ZrO_2} RT \ln \frac{x_{ZrO_2}}{1 + x_{Gd_2O_3}} + 2x_{Gd_2O_3} RT \ln \frac{2x_{Gd_2O_3}}{1 + x_{Gd_2O_3}}, \quad (2)$$

where x_{ZrO_2} and $x_{Gd_2O_3}$ are the mol fractions of ZrO_2 and Gd_2O_3, respectively. The ideal mixing term for the distribution of O^{2-} ions and vacancies has been neglected since the distribution of oxide vacancies is related to the RE^{3+} position in the lattice structure. The ideal mixing term overlooks the thermal effects associated with mixing. To adjust the Gibbs energy for any departure from the ideal term, an excess (G^E) term is added. The excess Gibbs energy may be represented (for a 1 mol solution of ZrO_2–$GdO_{1.5}$) by [6,10]:

$$G^E = p_o x_{ZrO_2} x_{GdO_{1.5}}, \quad (3)$$

where p_o may be a function of temperature. For a 1 mol solution of ZrO_2–Gd_2O_3, the excess mixing term is equally represented by:

$$G^E = 2p_o x_{ZrO_2} x_{Gd_2O_3} \quad (4)$$

The Gibbs energy curves can then be constructed for the cubic-fluorite and liquid phases at 2773 K and 0.1 MPa as functions of $x_{GdO_{1.5}}$ with an appropriate value of p_o for each phase. Combined with knowledge of the Gibbs energy difference between the cubic-fluorite and liquid phases of the pure component oxides, the Gibbs energy curves for the cubic-fluorite and liquid phases appear as shown in Fig. 1.

The methodology of Gibbs energy minimization implies that the phase with the lowest Gibbs energy at a given temperature and composition is most stable at equilibrium conditions. It is to be noted that, between the lines of common tangency running from 0.57 to 0.71 $x_{GdO_{1.5}}$, two phases are slightly more stable than either one separately. This is to be compared with Fig. 2 at 2773 K.

This thermodynamic methodology can be expanded to include all of the other possible phases present in the binary system (e.g., monoclinic, hexagonal, tetragonal, bixbyite, as well as the stoichiometric compounds). Excess mixing parameters are tuned to provide selected critical features in previously published phase diagrams. This approach does not preclude using measurements of the Gibbs energy of mixing or related properties but sufficient information of this type with the high accuracy required is not currently available.

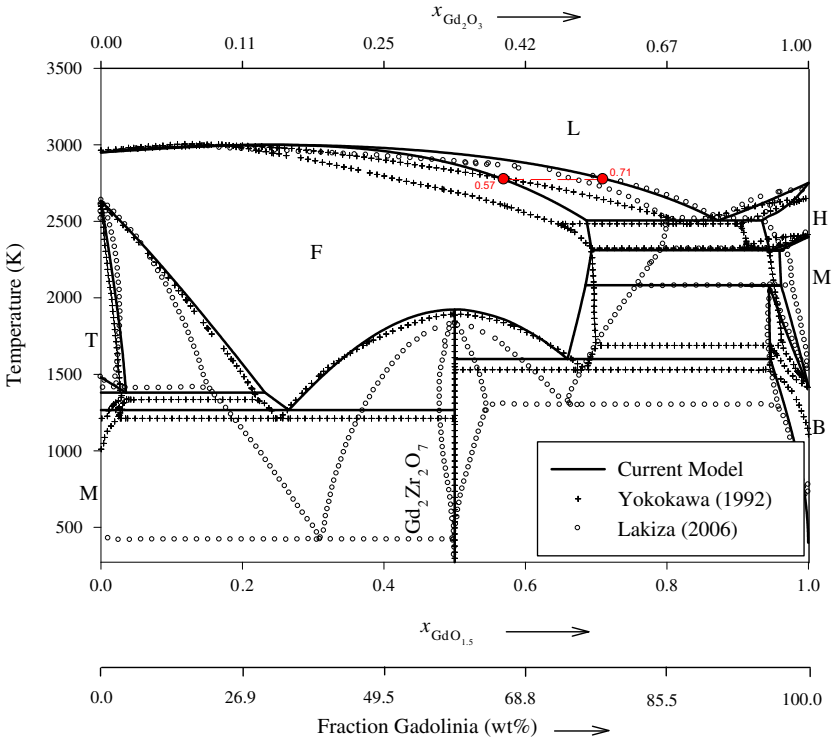

Fig. 2. Zirconia–gadolinia binary model developed for the BNA treatment. A comparison of the treatments proposed by Yokokawa [11] and Lakiza [12] are both shown. Note, B, F, H, L, M, T represents bixbyite, fluorite, hexagonal, liquid, monoclinic, and tetragonal phases, respectively.

3. BNA binary systems

The three binary subsystems with ZrO_2 (Figs. 2–4) were modelled to follow previous diagrams found in the literature. A comparison between BNA binary subsets is presented and discussed. The computed diagrams utilized as few modeling parameters as possible to represent each phase. The binary diagrams follow the general profile of previously published phase diagrams to fidelity

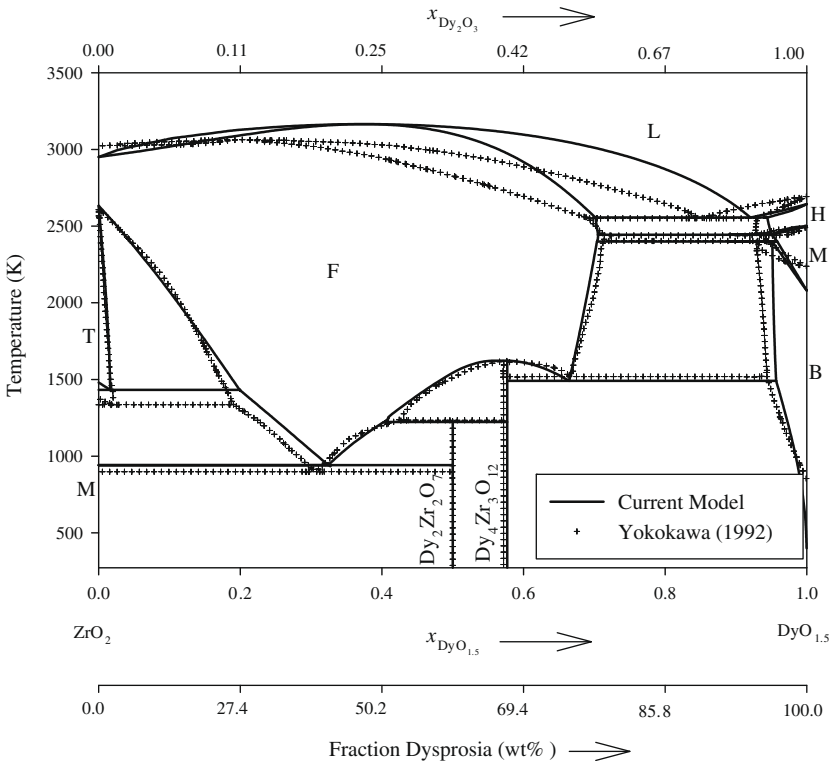

Fig. 3. Zirconia–dysprosia binary model developed for the BNA treatment. A comparison of the binary system proposed by Yokokawa is also shown [11]. Note, B, F, H, L, M, T represents bixbyite, fluorite, hexagonal, liquid, monoclinic, and tetragonal phases, respectively.

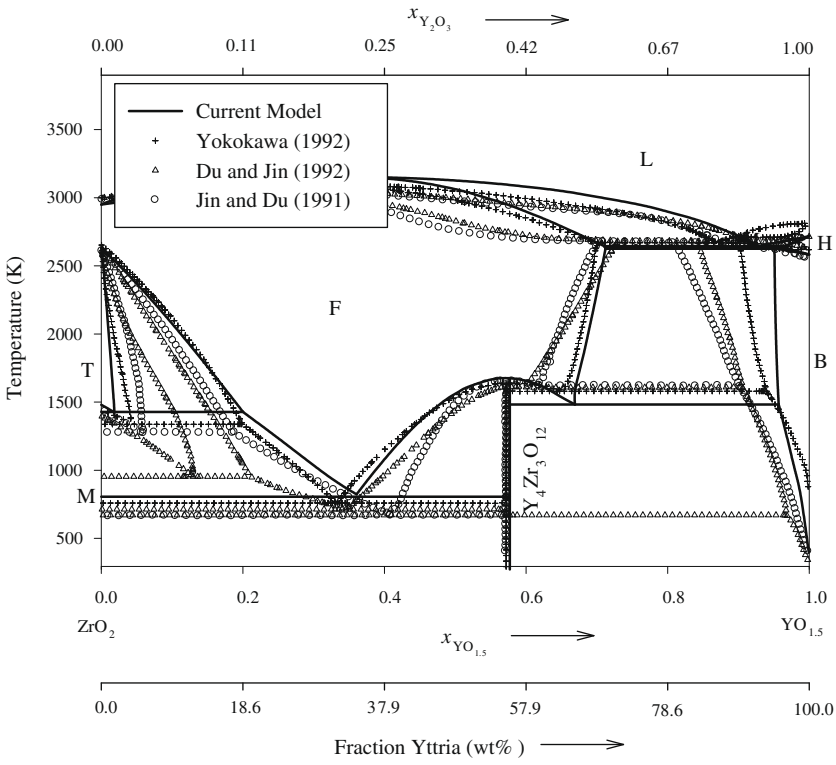

Fig. 4. Zirconia–yttria binary model developed for the BNA treatment. A comparison of the binary system proposed by Yokokawa [11], and Jin and Du [14,15] are also shown. Note, B, F, H, L, M, T represents bixbyite, fluorite, hexagonal, liquid, monoclinic, and tetragonal phases, respectively.

in keeping with the uncertainty of these diagrams. The thermodynamic constants are summarized in Tables 1 and 2.

The zirconia–gadolinia phase diagram (Fig. 2) is an amalgamation of both the Yokokawa [11] and Lakiza [12] treatments. The

Table 1
Thermodynamic constants for components of current treatment.

Compound	Phase	T_{min} (K)	T_{max} (K)	G^o (J mol^{-1}) Calculated for T(K) at 0.1 MPa	Ref.
ZrO_2	Monoclinic	298	1478	$-1106167.259 + 652.5882799T - 2337.903220T^{*0.5} + 20068472.32T^{-2.0} - 94.62116000T\ln(T)$	[16,17]
		1478	2950	$-1121304.040 + 454.9897036\ T - 74.47520000T\ln(T)$	
		2950	3500	$-1160801.000 + 575.3491305T - 87.86400000T\ln(T)$	
	Tetragonal	298	2950	$-1115350.775 + 450.9688566T - 74.47520000T\ln(T)$	
		2950	3500	$-1154847.735 + 571.3282835T - 87.86400000T\ln(T)$	
	Fluorite	298	2950	$-1104765.778 + 446.9488568T - 74.47520000T\ln(T)$	
		2950	3500	$-1144262.738 + 567.3082838T - 87.86400000T\ln(T)$	
	Liquid	298	3500	$-1057215.647 + 537.8074690T - 87.86400000T\ln(T)$	
	Bixbyite*	298	3500	$G^o(ZrO_2$ monoclinic$) + 14000$	
	Hexagonal*	298	3500	$G^o(ZrO_2$ fluorite$) + 7000$	
	RE-rich monoclinic*	298	3500	$G^o(ZrO_2$ monoclinic$) + 15000$	
Gd_2O_3	Bixbyite	298	2683	$-1858030.935 + 620.3162941T - 0.7234136000E\text{-}02T^{*2.0} + 541200.4000T^{-1.0} - 114.4909760T\ln(T)$	[11–13,16,17]
	RE-rich monoclinic	298	3000	$-1856607.982 + 619.3163181T$ - $0.7234136000E\text{-}02T^{*2.0} + 541200.4000T^{-1.0} - 114.4909760T\ln(T)$	
	Hexagonal	298	3000	$-1842248.494 + 613.3290141T - 0.7234136000E\text{-}02T^{*2.0} + 541200.4000T^{-1.0} - 114.4909760T\ln(T)$	
	Liquid	298	2683	$-1803697.118 + 598.7686941T - 0.7234136000E\text{-}02T^{*2.0} + 541200.4000T^{-1.0} - 114.4909760T\ln(T)$	
	Tetragonal*	298	2683	$G^o(Gd_2O_3$ bixbyite$) + 10000$	
	Fluorite*	298	2683	$G^o(Gd_2O_3$ bixbyite$) + 20000$	
Dy_2O_3	Bixbyite	298	3000	$-1903060.583 + 671.4629379T - 0.7638045000E\text{-}02T^{*2.0} + 422900.0000T^{-1.0} - 121.2302000T\ln(T)$	[11,13,16,17]
	RE-rich monoclinic	298	3000	$-1900980.383 + 670.4629379T - 0.7638045000E\text{-}02T^{*2.0} + 422900.0000T^{-1.0} - 121.2302000T\ln(T)$	
	Hexagonal	298	3000	$-1885979.483 + 664.4629379T - 0.7638045000E\text{-}02T^{*2.0} + 422900.0000T^{-1.0} - 121.2302000T\ln(T)$	
	Liquid	298	3000	$-1847566.083 + 649.9297379T - 0.7638045000E\text{-}02T^{*2.0} + 422900.0000T^{-1.0} - 121.2302000T\ln(T)$	
	Tetragonal*	298	3500	$G^o(Dy_2O_3$ Bixbyite$) + 5000$	
	Fluorite*	298	3500	$G^o(Dy_2O_3$ bixbyite$) + 22500$	
Y_2O_3	Bixbyite	298	3000	$-1944687.977 + 783.5556567T - 131.7960000T\ln(T)$	[11,15–18]
	Hexagonal	298	3000	$-1902285.577 + 767.1397063T - 131.7960000T\ln(T)$	
	Liquid	298	3000	$-1833377.577 + 741.7872412T - 131.7960000T\ln(T)$	
	Tetragonal*	298	3000	$G^o(Y_2O_3$ bixbyite$) + 7000$	
	Fluorite*	298	3000	$G^o(Y_2O_3$ bixbyite$) + 22500$	
$Gd_2Zr_2O_7$	Stoichiometric compound	298	2500	$-4136898.503 + 1514.214008T - 0.7234136000E\text{-}02T^{*2.0} + 541200.4000T^{-1.0} - 263.4413760T\ln(T)$	[11–13,16,17]
$Dy_2Zr_2O_7$	Stoichiometric compound	298	2500	$-4181294.145 + 1565.360652T - 0.7638045000E\text{-}02T^{*2.0} + 422900.0000T^{-1.0} - 270.1806000\ T\ln(T)$	[11,13,16,17]
$Y_2Zr_2O_7$	Stoichiometric compound	298	2500	$-4184269.128 + 1773.918943T - 1168.952000T^{*0.5} + 10000000.00T^{-2.0} - 290.8194000T\ln(T)$	[11,15–18]
$Gd_4Zr_3O_{12}$	Stoichiometric compound	298	2500	$-7020357.617 + 2581.468581T - 0.1445000000E\text{-}01T^{*2.0} + 1082401.000T^{-1.0} - 452.4076000T\ln(T)$	[11–13,16,17]
$Dy_4Zr_3O_{12}$	Stoichiometric compound	298	2500	$-7242805.509 + 2683.772447T - 0.1527609000E\text{-}01T^{*2.0} + 845800.0000T^{-1.0} - 465.8860000T\ln(T)$	[11,13,16,17]
$Y_4Zr_3O_{12}$	Stoichiometric compound	298	2500	$-7306838.119 + 2895.245460T - 487.0170000T\ln(T)$	[11,15–18]

* Indicates metastable phase used for the purpose of binary phase construction.

Table 2
Excess parameters for binary subsystems.

Phase	Component 1	Component 2 (0.5 RE_2O_3)	Binary excess parameter p_o (J mol^{-1})
Fluorite	ZrO_2 (fluorite)	Dy_2O_3 (fluorite)	−60000
	ZrO_2 (fluorite)	Gd_2O_3 (fluorite)	−45000
	ZrO_2 (fluorite)	Y_2O_3 (fluorite)	−60000
Tetragonal	ZrO_2 (tetragonal)	Y_2O_3 (tetragonal)	−2000
Liquid	ZrO_2 (liquid)	Dy_2O_3 (liquid)	−15000
	ZrO_2 (liquid)	Gd_2O_3 (liquid)	−20000
	ZrO_2 (liquid)	Y_2O_3 (liquid)	−10000
RE-rich monoclinic	ZrO_2 (RE-rich monoclinic)	Dy_2O_3 (RE-rich monoclinic)	−9000
Bixbyite	ZrO_2 (bixbyite)	Dy_2O_3 (bixbyite)	−11500
	ZrO_2 (bixbyite)	Gd_2O_3 (bixbyite)	−6000
	ZrO_2 (bixbyite)	Y_2O_3 (bixbyite)	−11500
Hexagonal	ZrO_2 (hexagonal)	Dy_2O_3 (hexagonal)	−1000
	ZrO_2 (hexagonal)	Gd_2O_3 (hexagonal)	+5000
	ZrO_2 (hexagonal)	Y_2O_3 (hexagonal)	+9750

Note: The $RE_2Zr_2O_7$ and $RE_4Zr_3O_{12}$ solutions are treated as ideal by assuming ideal mixing of the RE^{3+} ions.

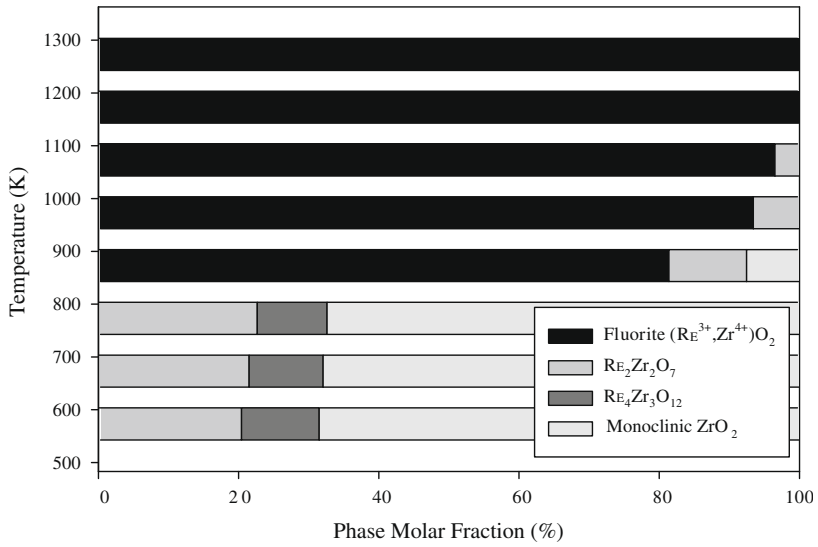

Fig. 5. Pseudo phase diagram for a 63 mol% ZrO_2, 15 mol% $YO_{1.5}$, 11 mol% $GdO_{1.5}$, and 11 mol% $DyO_{1.5}$ sample.

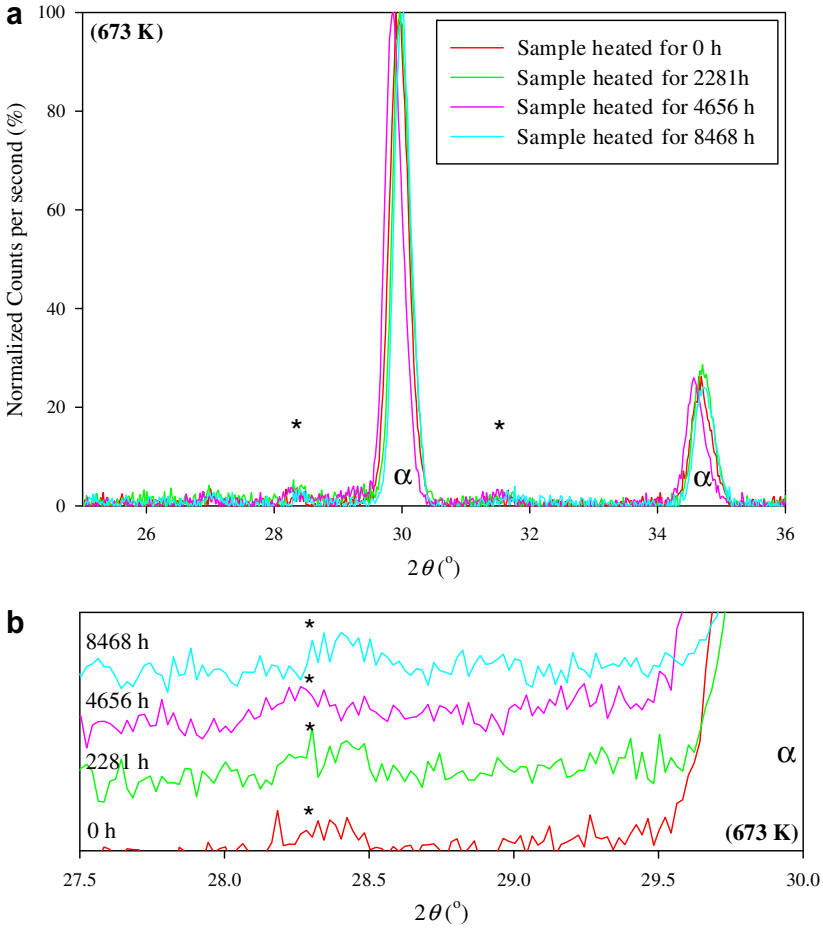

Fig. 6. Heat treatment results for a 63 mol% ZrO_2, 15 mol% $YO_{1.5}$, 11 mol% $GdO_{1.5}$, and 11 mol% $DyO_{1.5}$ sample heated at 673 K for one year. (a) is a complete scan of the sample at incremental times (0, 2281, 4656, and 8468 h); (b) is a staggered scan comparison of the profiles in the region of the ZrO_2 monoclinic peak. Note XRD scans have been normalized to the fluorite peak maximum ($2\theta \approx 30°$); (*) indicates the approximate location of the ZrO_2 monoclinic peaks [20]; (α) indicates the approximate location of the ZrO_2 fluorite peak [20].

treatment locates the eutectoid for the ZrO_2(monoclinic)–fluorite–$Gd_2Zr_2O_7$ (stoichiometric compound) at 1267 K, the ZrO_2(monoclinic)–ZrO_2(tetragonal)–fluorite eutectoid at 1381 K, the $Gd_2Zr_2O_7$–fluorite–bixbyite eutectoid at 1600 K, and the decomposition temperature of $Gd_2Zr_2O_7$ at 1923 K. The shape of the liquid–fluorite two phase region and RE-rich phase invariants at 2506,

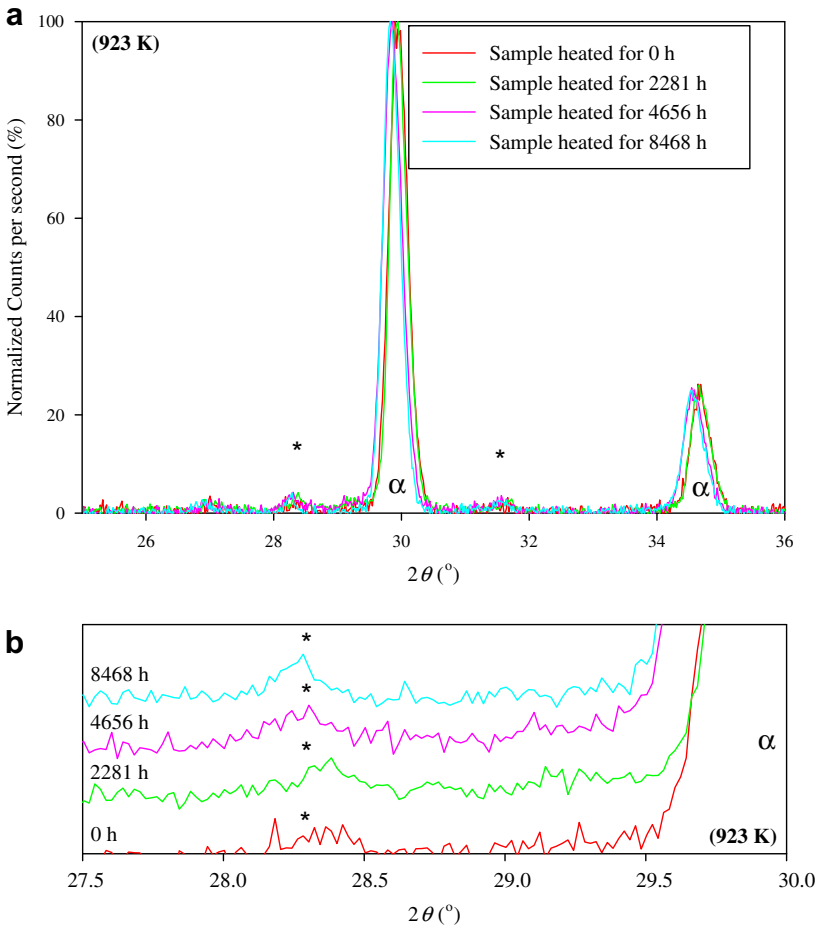

Fig. 7. Heat treatment results for a 63 mol% ZrO_2, 15 mol% $YO_{1.5}$, 11 mol% $GdO_{1.5}$, and 11 mol% $DyO_{1.5}$ sample heated at 923 K for one year. (a) is a complete scan of the sample at incremental times (0, 2281, 4656, and 8468 h); (b) is a staggered scan comparison of the profiles in the region of the ZrO_2 monoclinic peak. Note XRD scans have been normalized to the fluorite peak maximum ($2\theta \approx 30^o$); (*) indicates the approximate location of the monoclinic peaks [20]; (α) indicates the approximate location of the fluorite peak [20].

2311, and 2082 K are close to the Lakiza model (based upon experimental data) [12]. The lower eutectoids proposed by Lakiza between the ZrO_2(monoclinic)–cubic–$Gd_2Zr_2O_7$ and the $Gd_2Zr_2O_7$–fluorite–bixbyite are not followed as there is no actual data to support the location of these eutectoids as a result of poor kinetics at these temperatures. Lakiza also proposes a non-stoichiometric region for $Gd_2Zr_2O_7$. Again there are very little experimental data in this region to support the existence of this non-stoichiometric region; as such, it was not added to this treatment.

The zirconia–dysprosia phase diagram (Fig. 3) follows the treatment proposed by Yokokawa [11]. The ZrO_2(monoclinic)–fluorite–$Dy_2Zr_2O_7$ eutectoid is located at 942 K; the ZrO_2(monoclinic)–ZrO_2(tetragonal)–fluorite eutectoid is located at 1432 K. The RE-rich phase invariants are at 2556, 2444, 2399, and 1491 K. The phases $Dy_2Zr_2O_7$ and $Dy_4Zr_3O_{12}$ decompose at 1223 and 1624 K, respectively. It is of note that the liquid–fluorite two phase region does not follow that of Yokokawa. The current model matches the location of the eutectic at 2556 K; the resultant shape of the liquid–fluorite two phase region is a ripple effect of fitting the eutectic. The transition temperatures in pure Dy_2O_3 follow the transition temperatures proposed by White [13]: liquid to hexagonal at 2643 K, hexagonal to monoclinic at 2500 K and monoclinic to bixbyite at 2080 K.

The zirconia–yttria binary phase diagram (Fig. 4) follows Yokokawa [11] and the model of Jin and Du [15]. Both diagrams agree in the areas of the eutectic, eutectoids and the decomposition temperature of $Y_4Zr_3O_{12}$. For the current treatment, the ZrO_2(monoclinic)–fluorite–$Y_4Zr_3O_{12}$ eutectoid is located at 805 K, the ZrO_2(monoclinic) tetragonal–fluorite eutectoid is at 1428 K, and the RE-rich eutectic and eutectoids are located at 2645, 2629, and, 1482 K. The decomposition temperature for $Y_4Zr_3O_{12}$ is 1676 K.

4. Estimated phase equilibrium of the quaternary system

The parameters needed to generate the three phase diagrams in Figs. 2–4 were incorporated into one overall treatment by the interpolation method attributed to Toop [19], where the mixing of the ions (RE^{3+}) in the binary systems is assumed to be ideal. The phases and their proportions for illustration were computed at a composition of 63 mol% ZrO_2, 15 mol% $YO_{1.5}$, 11 mol% $GdO_{1.5}$, and 11 mol% $DyO_{1.5}$ over a range of temperatures. The results are represented in a bar graph in Fig. 5. The situation showing three phases over a range of temperatures at 900 K and below is a consequence of additional degrees of freedom for a system with more than two components.

To prepare the BNA material for insertion into the fuel bundle, the BNA material is sintered in the cubic-fluorite region (above 1200 K for a 63 mol% ZrO_2, 15 mol% $YO_{1.5}$, 11 mol% $GdO_{1.5}$, and 11 mol% $DyO_{1.5}$ sample). As illustrated in Fig. 5, below 900 K (possible range of operational conditions for this material in an ACR fuel bundle), BNA material of this composition will likely be most

stable not as a fluorite phase but as monoclinic–ZrO_2 and both stoichiometric compounds ($RE_2Zr_2O_7$ and $RE_4Zr_3O_{12}$).

5. Estimated phase equilibrium of the quaternary system

To judge the rate at which the BNA material converts from a completely fluorite phase to monoclinic–fluorite two phase system, long term heat treatments over the course of a year were completed. The sample was prepared by mechanically blending oxide powders, pressing and sintering at 1873 K. The sintered samples were then crushed and sieved through a 500 μm screen. The powdered samples were heated at 673, 773, 848, and 923 K under atmospheric conditions for approximately one year. Periodic evaluation of the samples was undertaken by X-ray diffraction (XRD) using a Scintag X1 X-ray diffractometer (with a Cu target). The scans were from $2\theta = 25–36^{\circ}$ at 0.1 min^{-1} (where θ is the Bragg angle). The results for the 673 and 923 K heat treatments are summarized in Figs. 6 and 7, respectively, and are indicative of the results at 773 and 848 K.

As illustrated in Figs. 4 and 5, as the heat treatment continues, the monoclinic peak slightly matures. This degradation from a single fluorite phase to a monoclinic–fluorite two phase mixture is consistent with the BNA thermochemical model at 673 and 923 K, respectively, (Fig. 4). Given the relative size of the monoclinic peaks compared to the fluorite peak, it is inferred that the rate of this degradation is slow and increases slightly with temperature as illustrated in Figs. 6a and 7a. Four samples of similar compositions have been tested in a similar manner. These samples show little to no maturation of a monoclinic–fluorite two phase mixture after heating at 673 and 923 K for approximately six months.

6. Summary

This work describes thermodynamic modelling treatments for the binary temperature – composition phase diagrams of zirconia–gadolinia, zirconia–dysprosia, and zirconia–yttria. These were incorporated into a quaternary model capable of predicting the phase stability of the burnable neutron absorbing materials as a function of temperature. Supporting XRD experimentation was undertaken. It was found that thermochemical model predictions were consistent with experimental results. The rate of phase development from a single cubic-fluorite phase to a monoclinic phase mixture was slow (even after months of heating at temperatures higher then expected in actual service).

Acknowledgements

The authors thank P. Boczar, L. Dickson, R. Verrall, J. Mouris, and H. Hamilton of AECL for their continued support and encouragement. The authors wish to call attention to the important contributions of the late Faramarz Akbari, which extended into many subject areas related to this project.

References

[1] C. Degueldre, J.M. Paratte, J. Nucl. Mater. 274 (1999) 1.
[2] C. Degueldre, T. Yamashita, J. Nucl. Mater. 319 (2003) 1.
[3] C. Degueldre, Ch. Hellwig, J. Nucl. Mater. 320 (2003) 96.
[4] Ch. Hellwig, M. Streit, P. Blair, T. Tverberg, F.C. Klaassen, R.P.C. Schram, F. Vettraino, T. Yamashita, J. Nucl. Mater. 352 (2006) 291.
[5] M. Streit, T. Tverberg, W. Wiesenack, F. Vettraino, J. Nucl. Mater. 352 (2006) 263.
[6] A.D. Pelton, W.T. Thompson, Prog. Sol. Stat. Chem. 10 (1975) 119.
[7] E.C. Corcoran, B.J Lewis, W.T. Thompson, Computed phase equilibria for burnable neutron absorbing materials for the advanced CANDU reactor design, in: Proceedings of 29th Canadian Nuclear Society Conference, June 2008.
[8] J. Hood, F. Akbari, Z. He, P. Reid, E.C. Corcoran, B.J Lewis, W.T. Thompson, ZrO_2–RE_2O_3 phase stability program in support of ACR-1000® fuel design, in: Proceedings of 29th Canadian Nuclear Society Conference, June 2008.
[9] W.T. Thompson, A.D. Pelton, C.W. Bale, Facility for the Analysis of Chemical Thermodynamics ($F^*A^*C^*T$) McGill – Ecole Polytechnique, 2003.
[10] C.H.P. Lupis, Chemical Thermodynamics of Materials, Elsevier Science Publishing Co., Inc., New York, 1983.
[11] H. Yokokawa, N. Sakai, T. Kawada, M. Dokiya, Phase diagram calculations for ZrO_2 based ceramics: thermodynamic regularities in zirconate formation and solubilities of transition metal oxides, in: S.P.S. Badwal, M.J. Bannister, R.H.J. Hannink (Eds.), Science and Technology of Zirconia V, Technomic Publishing, Lancaster (PA), 1990, pp. 59–68. Republished in the ACRs-NIST Phase Equilibrium Diagram Database, V3.0, American Ceramics Society (2004).
[12] S. Lakiza, O. Fabrichnaya, Ch. Wang, M. Zinkevich, F. Aldinger, J. Euro. Ceram. Soc. 26 (2006) 233.
[13] S.J. White, Master's Thesis, Royal Military College of Canada, Kingston, Ontario, Canada, 2006.
[14] Z. Jin, Y. Du, CALPHAD 16 (1992) 355.
[15] Y. Du, Z. Jin, P. Huang, J. Am. Ceram. Soc. 74 (1991) 1569.
[16] A.D. Pelton, G. Eriksson, P. Wu, Phas. Diag. Ceram. 10 (1993).
[17] I. Barin, Thermochemical Data of Pure Substances, VCH, Weinheim, Germany, 1989.
[18] M. Medraj, R. Hammond, W.T. Thompson, R.A.L. Drew, Can. Matal. Quart. 42 (2003) 495.
[19] G.W. Toop, Trans. Am. Inst. Min. Met. Petro. Eng. 233 (1965) 850.
[20] N.R. Rebollo, O. Fabrichnaya, C.G. Levi, Z. Metallkd. 94 (2003) 163.